100kV Electron Beam Lithography System: JBX-9300FS

Hirofumi Ohki and Hitoshi Takemura

Semiconductor Equipment Division, JEOL Ltd.

Spot electron-beam(e-beam) lithography systems are promising equipment for fabrication and research of sub-100nm size devices. And, adding to the conventional applications such as fabrication of high speed transistors or optical devices, new demands for higher voltage lithography for X-ray or e-beam projection mask making have been increasing.

Now, sub-50nm size fabrication is aimed at and the required writing accuracy will increase as feature sizes decrease. To play an important role in next generation device fabrication, we have developed the JBX-9300FS, a 100kV spot e-beam lithography system.

In this paper we introduce the JBX-9300FS in terms of system implementation, performance, and writing results.

1. Introduction

The JBX-9300FS is a 100kV spot e-beam lithography system for fabricating sub-100 nm size devices and masks of X-ray or e-beam projection lithography[1].

We describe its system specifications and key technologies to achieve high accuracy writing.

2. System Specifications of the JBX-9300FS

We show the system specifications in **Table 1**. The JBX-9300FS employs a ZrO/W emitter for forming a spot beam, a vector-scanning system, and step & repeat stage-movement system.

Adapting to the increase of writing material sizes, we have made it possible to load wafers up to 300 mm and mask blanks up to 230 mm.

Accelerating voltage can be switched from 50 (100) kV to 100 (50) kV.

Field size is 1000μm at 50kV and 500μm at 100 kV.

We have employed a two-stage electrostatic deflector system, to increase the writing speed adapting to the high sensitivity e-beam resists.

Critical dimension (CD) uniformity within a writing field has been improved by dynamic focus and astigmatism correction. And writing accuracy has been increased by employing some new technologies for height correction, signal processing, and mark alignment in direct writing.

3. System Implementation of the JBX-9300FS

Figures 1 shows the external view of JBX-9300FS, **Figures 2** the electron optics system, and **Figures 3** the block diagram of the control system.

3.1. Electron Optics System

As shown in Fig.2, an electron source image at a ZrO/W emitter is optically demagnified

Accelerating voltage	100 kV	50 kV
Max. field size	500 μm	1000μm
Max. sub-deflection size	4 μm	8μm
Min. beam size	4 nm	7 nm
Address unit	1 nm	2 nm
Laser resolution	/1024=0.6 nm	Same as left
Main deflection DAC	20 bit	Same as left
Sub-deflection DAC	12 bit	Same as left
Max. scanning speed	25 MHz	Same as left
Writing area	230 mm× 230 mm	Same as left
Loadable-wafer size	300 mm	Same as left
Loadable-mask size	230 mm	Same as left
Stitching accuracy	20 nm	25 nm
Overlay accuracy	25 nm	30 nm
Positional accuracy within material surface	30 nm	30 nm
Min. writing linewidth	20nm	35 nm

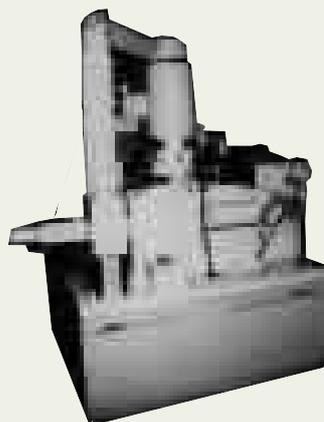Table 1. Basic specifications for JBX-9300FS

Fig.1. External view of JBX-9300FS.

and projected to the writing plane.

Generated electron beam is accelerated to 50 kV or 100 kV through the four-stage accelerating electrodes. This accelerating field plays the role of an electrostatic lens, and the first crossover is formed at the center position of the split blanking electrodes.

Two condenser lenses work as zoom lens, which means that the 3rd condenser lens value is set up linked to the 2nd lens value, in order to project a demagnified image onto the fixed point as the third crossover.

Finally, the objective lens projects the third crossover onto the writing plane as a spot beam.

3.2. Deflection System

We have employed a two-stage electrostatic deflector system adapting to a high resolution and high sensitivity e-beam resists.

One is the deflector that designates writing positions (positioning deflector), and the other is the deflector that writes patterns rapidly (writing deflector).

The positioning deflector consists of octopole cylindrical electrodes and is located in the objective lens. It uses 20-bit DACs.

The writing deflector, on the other hand, consists of quadrupole cylindrical electrodes and is located above the objective lens. It uses 12-bit DACs.

Furthermore, we have implemented two electrodes to improve the writing uniformity within a writing field correcting deflection aberration and astigmatism.

The former works for dynamic focus correction and the latter works for dynamic astigmatism correction.

These correction values are revolved in a writing field using third-degree polynomial and they are supplied as a correction voltage in pattern writing.

3.3. Signal Detection Systems

The signal detection systems we have newly developed are the height correction, backscattered electron (BE) signal processing, and absorbed electron (AE) signal processing.

The purposes of height measurement are corrections of objective lens focusing, deflection amplitude and rotation of main- and sub-deflectors.

Two pairs of height measurement systems detect height difference between the height standard plane on the stage and writing plane. And acquired height fluctuation is fed back to the focusing and deflection control unit.

BE signal is used for mark position determination and correction of deflection amplitude and rotation of main- and sub-deflectors. Detected signals from alignment marks in direct writing are also processed as BE signals.

The BE signal processing unit consists of BE signal detectors and the signal processing system. Detected digital BE signal is processed by correlation operation and a mark position is determined from the top peak signal position.

$$g(i) = \sum_{j=1}^{n} f(i \quad j) \ f(i+j)$$

where $f(i)$ is detected signal, $-j \sim j$ is calculation range of correlation operation, and $g(i)$ is correlation operation processed signal.

Practical mark detection signals in direct writing (from top: raw signal, differential signal, correlation operation processed signal) are shown in **Figures 4**.

AE signal is mainly used for focus adjustment at the focus standard plane.

The AE signal processing unit consists of mesh marks with the role of knife edge, e-beam detectors below the meshes, and the signal processing system.

Detected digital AE signal when e-beam passes across a mesh mark is fitted to an error function, and a beam size is defined from coefficients of the error function.

Adding to the beam size measurement function, an automatic focus adjustment function to minimize a beam size is attached.

3.4. Chip Mark Alignment Method

Some wafers used in direct writing have some distortions such as warping, expanding, and shrinking through several thermal pre-processes.

To compensate these distortion influences on writing accuracies, four chip marks provided around a writing chip are detected for measuring how the chip region is distorted.

Assuming the designed mark coordinates as (x_i, y_i) (i=1~4) and the actual mark coordinates including wafer distortion as (X_i, Y_i) (i=1~4), we have the equations shown below.

$$X_i = A_0 + A_1 \quad x_i + A_2 \quad y_i + A_3 \quad x_i \quad y_i$$

$$Y_i = B_0 + B_2 \quad x_i + B_1 \quad y_i + B_3 \quad x_i \quad y_i$$

Solving these equations, we can obtain the distortion coefficients A_j (j=0~3), B_j (j=0~3).

By using these coefficients, the designed coordinates of field corners f_j (i=1~4) shown in **Figures 5** can be converted to f_i (i=1~4). Here the equations showing the conversion of f_j f_i are obtained in the same manner as for the distortion mentioned above. Actual writing positions are then determined using the conversion coefficients for f_j f_i.

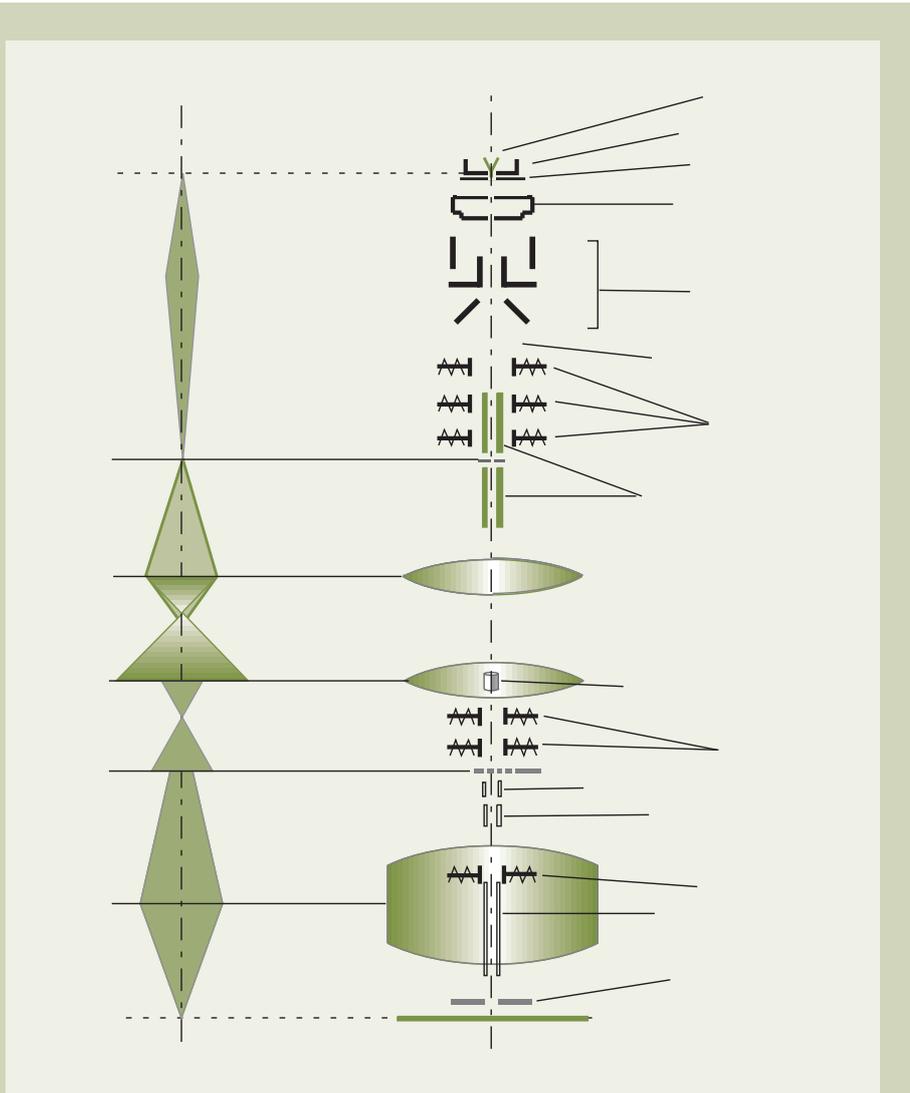The pattern writing program send these coefficients to the hardware arithmetic unit.

Fig.2. Electron optics system of JBX-9300FS.

Labels in figure: Electron Gun; ZrO/W; Suppressor; 1st anode; 2nd anode; Acceleration Electrode; Ground Anode; Aligner; Aperture; Blanking Plate; 2nd Lens; Demagnification Lens (Zooming Work); 3rd Lens; Dynamic Focus Correction Lens; Aligner; Aperture; Dynamic Stigmator; Scanning DEF; Objective Lens; Stigmator; Position DEF; Substrate; BE Detector

Then this hardware calculates compensated writing positions using coefficients and pattern writing goes on.

When one field writing is completed, the next coefficients are sent and the next field writing starts.

Repeating this procedure over the entire writing chip, direct writing is achieved with high accuracy.

4. Writing Results

Figures 6 and **7** show results of line and space pattern writing on ZEP520 (40 nm thick) on Si. Accelerating voltage is 100 kV and beam current is 100 pA. Line width of 15 nm in the X direction and 17 nm in Y direction have been attained.

5. Conclusion

It has been ascertained that high-accuracy writing results were obtained by employment of some technologies such as improvement of address unit resolution, newly developed signal processing systems, and dynamic correction within a writing field.

6. Acknowledgments

References

1. Y. Ochiai, H.Takemura et al. PERFORM-ANCE OF NEW E-BEAM LITHOG-RAPHY SYSTEM JBX-9300FS *Micro-and-nano-engineering* 99, pp147-148, 1999
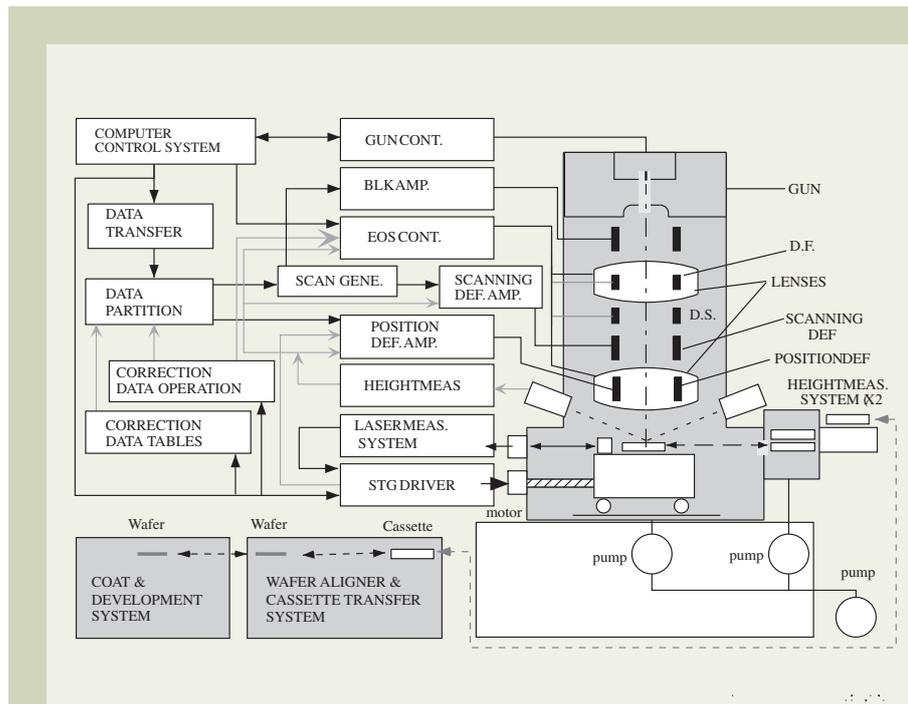

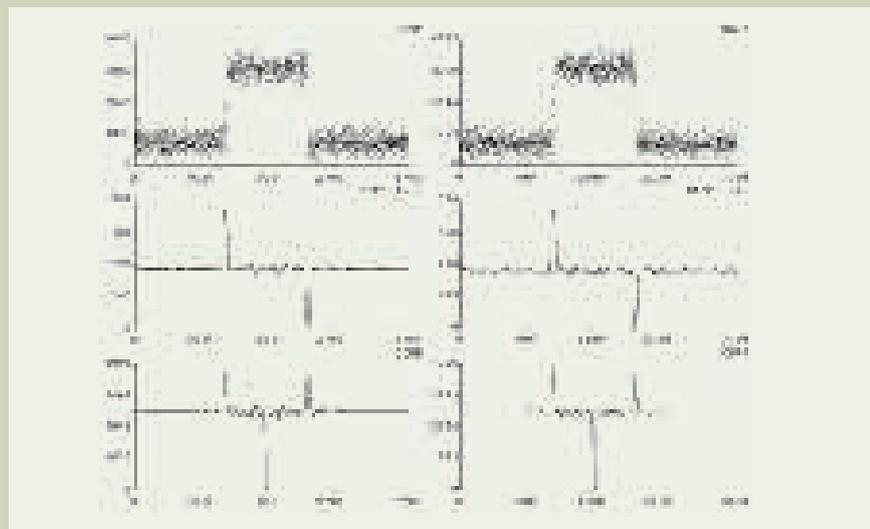Fig.3. Block diagram of the JBX-9300FS's control system.

Fig.4. Mark detection signals.

(M1-M4): Region defined by the designed four chip marks
(M1´-M4´): Region defined by the actual four chip marks

O : Average coordinate of the designed four chip marks.
f1-f4 : Designed field shape.
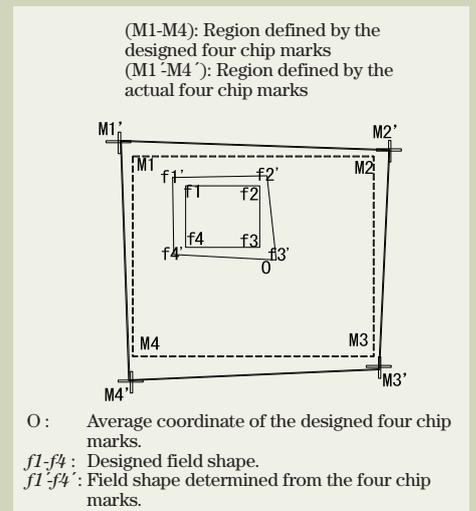f1´-f4´ : Field shape determined from the four chip marks.

Fig.5. 4-chip marks alignment.

Fig.6. X-direction line and space pattern writing (15nm)

Fig.7. Y-direction line and space pattern writing (17nm)

Gate Oxide Characterization using Annular Dark Field Imaging

D. A. Muller, F. H. Baumann

Bell Labs, Lucent Technologies

Modern integrated circuits can contain transistors smaller than 100 nm and gate oxides as thin as 2 nm. As a 0.1 nm decrease in oxide thickness can lead to an order of magnitude increase in leakage current, precise measurement of the oxide thickness is critical. We find annular dark field imaging in a scanning transmission electron microscope to be a useful method of measuring the thickness and roughness of a gate oxide. Thickness measurements are still possible in cross-sectioned samples as thick as 6000 Å. Imaging of dopant atom distributions is also possible, sometimes with single atom sensitivity.

In early 1999, a typical SiO_2 gate oxide was about 14 oxygen atoms thick. In early 2000, the oxide thickness had shrunk to 8 oxygen atoms. Between 2003 and 2008, the projected gate oxide thickness will be 4 oxygen atoms (1 nm). It is now technologically possible to produce nano-transistors with 5 oxygen-atom-thick gate oxides and 35 nm channel lengths [1]. Nevertheless, there are serious technological challenges that face the semiconductor industry if large-scale integrated circuits are to be manufactured using such devices [2]. The aggressive scaling of the gate dielectric presents challenges in controlling reliability, leakage and drive currents. The leakage due to direct tunneling through an SiO_2 gate oxide increases by roughly an order of magnitude for every Angstrom decrease in thickness [1]. The motivation for reducing the oxide thickness is to increase the electric field in the channel, thereby increasing the drive current. However as the electric field is increased above 1 MV/cm, the mobility is reduced due to surface roughness scattering. This is reflected in a decrease in drive current in transistors with gate oxides thinner than 1.3-1.5 nm for the smoothest Si/SiO_2 interfaces [1,3]. Consequently precise measurement and control of the oxide thickness and roughness is essential. Annular dark field (ADF) imaging offers quantitative measures of oxide thickness and roughness even when conventional high-resolution transmission electron microscopy (HRTEM) is beset with imaging artifacts.

A further complication is that the $Si-SiO_2$ interface is not atomically abrupt. For such thin devices even a 1 monolayer-thick suboxide can represent 40 % of the gate oxide thickness (since there are 2 Si/SiO_2 interfaces). Using atomic-scale electron energy loss spectroscopy

Murray Hill, NJ 07974. U.S.A

(EELS) [4] and *ab-initio* electronic structure calculations [5, 6], it has been shown that the *electrical* transition region from Si to SiO_2 occurs over a region that is 0.3-0.4 nm wide, even when the *structural* transition is atomically abrupt. The electrical and optical properties of the interfacial region are dramatically different from the bulk properties, but can be probed using EELS [4]. Thickness measurements are still possible using annular dark field (ADF) imaging as will be discussed here.

A second set of challenges facing device designers is the positioning and activation of dopant atoms. As devices shrink, the dopant concentrations in the source and drain must increase to ensure good contact to the transistor. Such concentrations can already exceed the solid solubility limits and are rapidly approaching the 1-% level. Locating individual dopant atoms with atomic resolution is certainly within the capabilities of ADF imaging [7, 8].

In this paper we discuss the use of a JEOL 2010F, operated as a scanning transmission electron microscope (STEM), for measuring dopant distributions and gate oxide thicknesses. Electronic properties of the Si/SiO_2 interface were measured using EELS. The microscope was fitted with the analytical (C_s=1 mm) polepiece, JEOL ADF detector, Gatan imaging filter and BF/ADF detectors. STEM images could be recorded with both the Emispec and Gatan systems.

In a scanning-transmission electron microscope (STEM), the atomic-resolution image formed by scanning an atom-wide electron beam and collecting the signal on an annular dark field detector can also be used to align and locate the small probe needed for electron-energy-loss spectroscopy. This makes it possible to measure the chemical composition and bonding of an interface with sub-nanometer spatial resolution [4, 9-11].

Apart from the manner in which the image is

formed (scanning versus parallel illumination), the main difference between ADF and HRTEM imaging is the contrast mechanism. For very thin specimens, HRTEM imaging is primarily a coherent, phase-contrast imaging technique while ADF imaging is an incoherent, amplitude-contrast technique[12-16]. **Figure 1** shows the contrast transfer functions (CTFs) for ADF and HRTEM images for the JEOL-2010F-ARP. The incoherent nature of the ADF image (which measures the square of the electron wave function) largely removes the contrast reversals present in phase-contrast HRTEM. ADF imaging also trades off higher resolution for reduced contrast. Consequently, raw ADF images always look more `blurry' than HRTEM images, which in turn are artificially sharpened by the microscope (The HTREM CTF removes the lower frequencies, while the ADF CTF enhances them). These models are no longer qualitatively correct for thicker specimens where multiple scattering is significant, but they still serve as a useful guide to the differences in image formation.

Figure 2 emphasizes the higher point-point resolution of incoherent imaging (roughly a factor of 40% better), showing the 1.63 Å spacing expected from figure 1. Note that antimony dopant atoms show up roughly nine times brighter than a silicon atom would - the cross section scales roughly as $Z^{1.7}$, so ADF imaging is sometimes known as "Z-Contrast" imaging [16], although not all contrast effects are related to atomic number alone. The effects of crystal orientation and strain fields can be pronounced [17], so it is always important to check the ADF result with an analytical technique such as EELS. This has been done for the case of antimony in silicon, where the ADF sensitivity is estimated to be +/- 0.5 atoms, and the EELS detection limit is +/- 2 atoms for a 100 kV VG-STEM [7]. We have succeeded in reproducing these experiments on the JEOL-
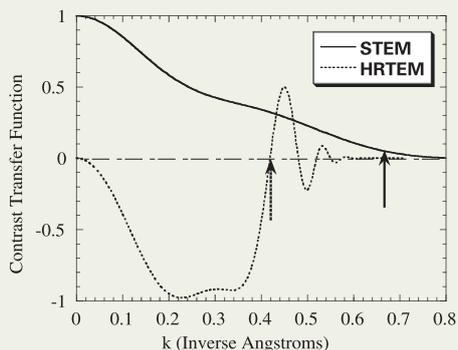
Fig.1. Contrast Transfer Functions (CTF's) for a JEOL 2010F operated in HRTEM mode (with a 0.7 mrad beam convergence) and ADF-STEM mode (with a 1 Å diameter source, and a 10 mrad probe forming aperture). The spherical aberration coefficient of the objective lens is 1.0 mm, a typical value for an analytical polepiece.The optimal focus is chosen for each mode. Note that there are contrast reversals in HRTEM mode, but not in STEM. The dashed arrow marks the Scherzer limit of 2.3 Å beyond which information in HRTEM mode can only be recovered by image reconstruction techniques. In ADF-STEM mode, information out to 1.5 Å (the solid arrow at k=0.666 Å^{-1}) can be directly interpreted. At this point the ADF-CTF has dropped to 5 % of its initial value, which is comparable to the noise levels in the image.
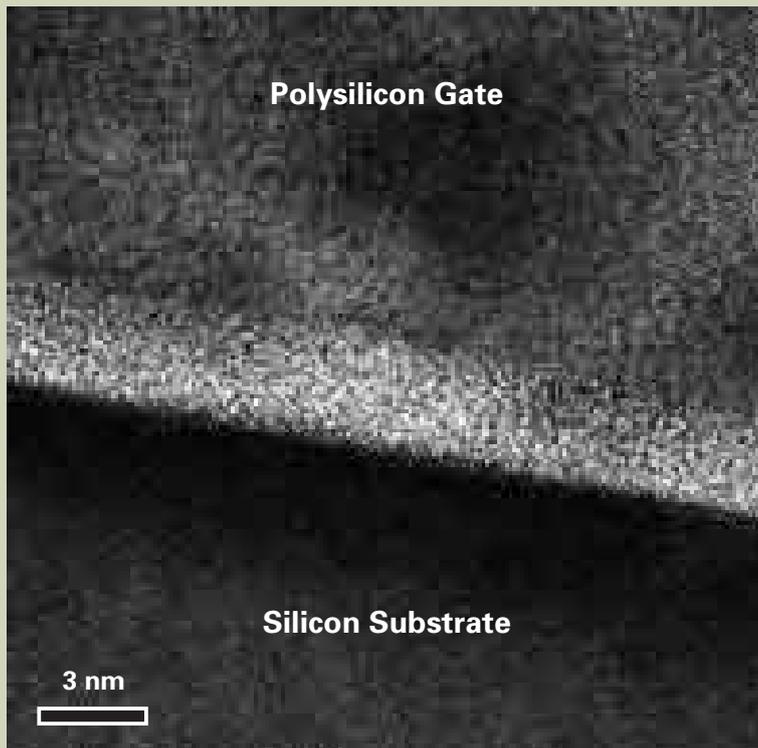

Fig.2. Annular dark field STEM image of an antimony delta-layer in [110] oriented Si, showing an information limit better than 0.163 nm, and minimal drift during the 40 second acquisition. The peak antimony concentration is 20 atoms or about 0.2 monolayers. (Digiscan and JEOL 2010F-ARP)
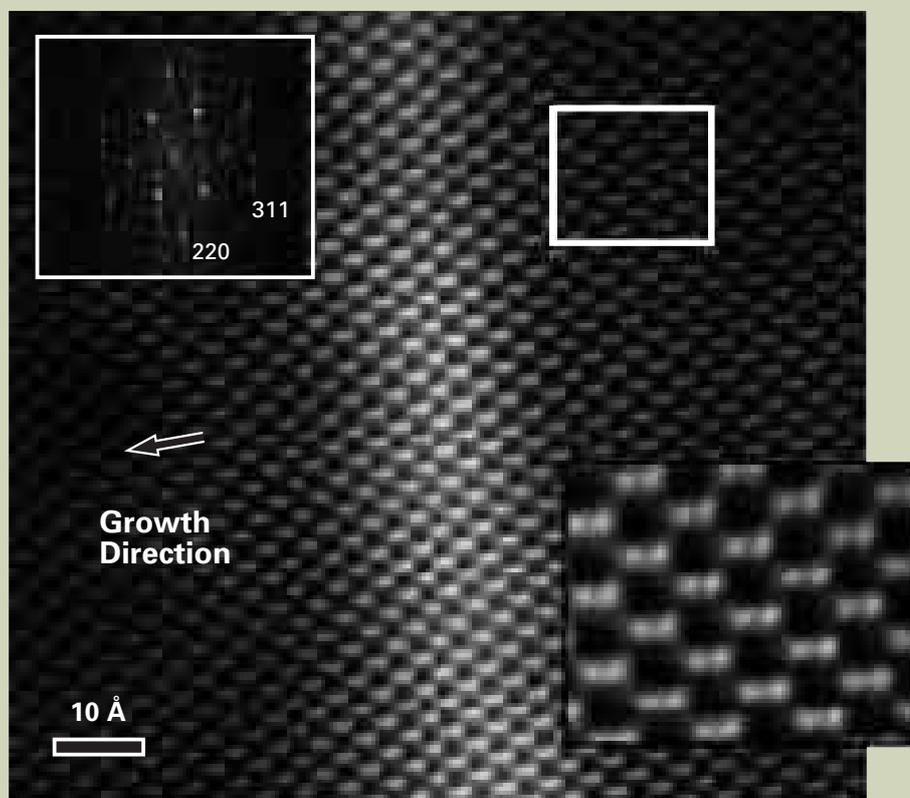

Fig.3. Bright Field STEM image of a gate oxide recorded with the Emispec system. The interface roughness was roughly 8 Å peak-peak (or 1.7 Å rms). The collection semi-angle was 1 mrad, and the probe forming aperture was 10 mrad semi-angle. (Emispec and JEOL 2010F-ARP)

2010F and find the sensitivity to be between 1 and 2 antimony atoms. Imaging As atoms has also proved practical. Light atoms, such as boron, can be imaged by reducing the ADF collector angle and imaging the strain field surrounding the dopant atoms. Single atom sensitivity for light elements in ADF is not yet possible at room temperature, but calculations suggest it should be possible with a liquid Nitrogen stage [8].

It should be noted that STEM is not exclusively restricted to ADF imaging. If a small collector (collector angle much smaller than the probe-forming aperture) is placed on axis, then the resulting bright field STEM image is formally equivalent to a conventional phase contrast HRTEM image. The collector angle in STEM plays an analogous role to the illumination angle in HRTEM. **Figure 3** shows a bright-field STEM image of a gate oxide, which would be hard to distinguish from a HRTEM image.

A serious limitation to all TEM imaging methods is that the sample is viewed in projection. All information along the path of the beam is collapsed into a single intensity measurement. Roughness is imaged differently in phase and amplitude contrast images, especially in thick samples. **Figure 4** shows the "black band" that is typically present in HRTEM images of Si/SiO$_2$ interfaces. (It is only in extremely thin samples that this band can be avoided). The EELS spectra on the left of the figure show that there is a substantial fraction of oxygen in the black band, as would be expected for a 6 Å peak-peak interface roughness. (This would correspond to a 1 Å rms roughness, which is typical). The "black band" is probably a more general case of dynamical diffraction artifacts seen in the roughness models of Akatsu and Odomhari [18]. Their work demonstrates that HRTEM images can make a rough interface appear quite smooth when the film thickness exceeds the roughness correlation length (typically 10-100 Å).

In contrast, ADF images degrade quite gracefully with thickness, displaying no dynamical diffraction artifacts (provided a large detector inner angle is used). **Figure 5** shows that the gate oxide thickness can be measured in specimens as thick as 6000 Å. Averaging of the roughness over the sample thickness still occurs in ADF imaging, so a rough interface will have a smooth edge, however the intensity of the bulk lattice will gradually fade away. The result is that the edge of the oxide does not appear to be well defined (since in projection it is not!). Fortunately, the incoherent nature of ADF imaging means that a line profile through the oxide will provide both the oxide thickness (from the full width at half maximum) and the roughness (convolved with the probe size). **Figure 6** shows the fit of a gaussian roughness profile to each interface. In general we find a good correspondence (within 10%) between x-ray and ADF measurements of interface roughness [4].

Some caveats are in order. As a scanned probe forms the ADF images, time-varying instabilities can lead to distortions in the image (which in HRTEM would only reduce the contrast). Spatial distortions over the field of view are almost always larger than 0.2 Å. Nevertheless, the almost-incoherent nature of ADF-image formation should make the method far
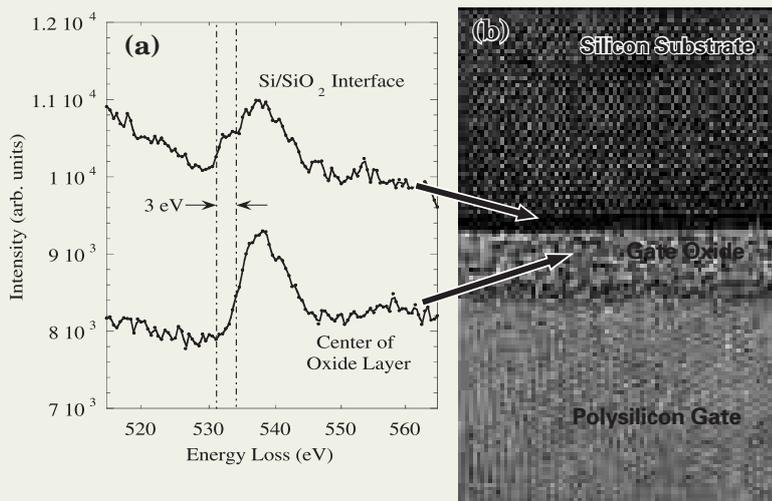

Fig.4. The HRTEM image recorded in the JEOL 2010F showing the 2 nm thick gate oxide and used to position the probe for spectroscopy. A Gatan imaging filter was used as the spectrometer, as the photodiode array of a conventional PEELS is not sensitive enough to detect the energy losses from a 20 pA, 0.2 nm sized probe. The interface states are visible as a pre-peak 3 eV below the O-K edge. This implies a reduced energy gap at the Si/SiO$_2$ interface [4].
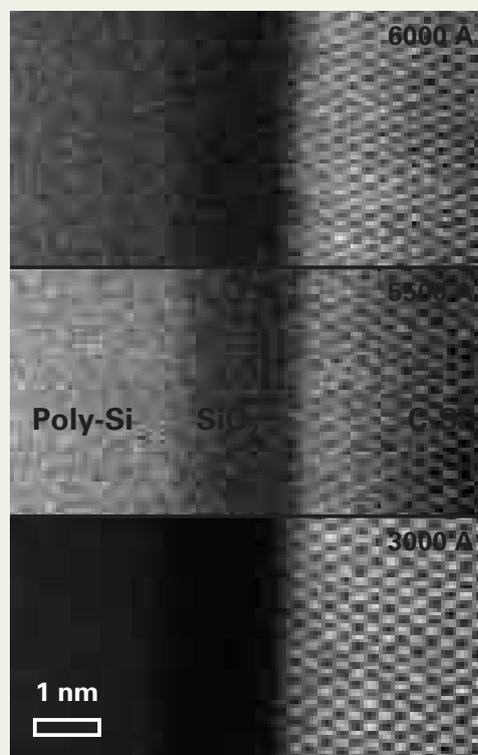
Fig.5. ADF images of a 2 nm gate oxide recorded at different sample thicknesses. The inner semi-angle on the ADF detector is 40 mrad and the probe forming aperture was 10 mrad semi-angle. The main effect of sample thickness is a reduction in signal/noise. The sample thickness was determined by EELS. (Digiscan and JEOL 2010F-ARP)

less sensitive to many of the problems experienced with phase-contrast HRTEM imaging. ADF images can only be formed over a much narrower range of specimen tilts than HRTEM images, reducing artifacts from misalignment of the crystal [15]. Contrast reversals with defocus are very much less likely to occur in ADF imaging, unless very large defocii or large objective apertures are used [15]. ADF images of crystals do not appear to reverse contrast with thickness as do HRTEM images [19], but they can do so at defects such as dislocations, in very thick films [17]. As in HRTEM, strain fields can complicate the image interpretation [17], but this can be minimized by using thin samples and large ADF collection angles.

In summary, ADF imaging has been demonstrated to provide quantitative information on the thickness and roughness of gate oxides. The images remain interpretable, even in thick samples. In the search for replacement gate dielectrics, the chemical sensitivity of ADF imaging is proving useful for quickly measuring reactions between silicon and the SiO_2 replacement.

References

1. G. Timp et al. (26 others), *IEDM Technical Digest* (1998) 615.
2. Semiconductor Industry Association, The National Technology Roadmap for Semiconductors (Sematech, Austin, 1997), 71-81.
3. G. Timp et al. (19 others), *IEDM Technical Digest* (1999) 55.
4. D. A. Muller, T. Sorsch, S. Moccio, F. H. Baumann and G. Timp, *Nature*, **399**, 758-761 (1999).
5. C. Kaneta, T. Yamasaki, T. Uchiyama, T. Uda, K. Terakura, *Microelectronic Engineering* **48** (1999) 117-120.
6. J. B. Neaton, N. W. Ashcroft, D. A. Muller, Phys. *Rev. Lett*. (in press)
7. P. H. Citrin, D. A. Muller, H.-J. Gossmann, R. Vanfleet and P. A. Northrup, *Phys. Rev. Lett*. **83** 3234 (1999).
8. S. Hillyard and J. Silcox, *Ultramicroscopy*, **58**, 6 (1995).
9. N. D. Browning and M. M. Chisholm and S. J. Pennycook, *Nature* **366**, 143 (1993).
10. D. A. Muller and Y. Tzou and R. Raj and J. Silcox, *Nature* **366**, 725 (1993).
11. P. E. Batson, *Nature* **366**, 728 (1993).
12. O. Scherzer, *J. Appl. Phys* **20**, 20 (1949).
13. E. Zeitler and M. G. R. Thomson, *Optik* **31**, 258 (1970).
14. G. Black and E. H. Linfoot, *Proc. Roy. Soc.* (London) **A239**, 522 (1957).
15. J. Silcox and P. Xu and R. L. Loane, *Ultramicroscopy* **47**, 173 (1992).
16. S. J. Pennycook, *Ultramicroscopy* **30**, 58 (1989).
17. D. D. Perovic and C. J. Rossow and A. Howie, *Ultramicroscopy* **52**, 353 (1993).
18. H. Akatsu, I. Ohdomari, *Applied Surf Science*, **41** 357 (1989).
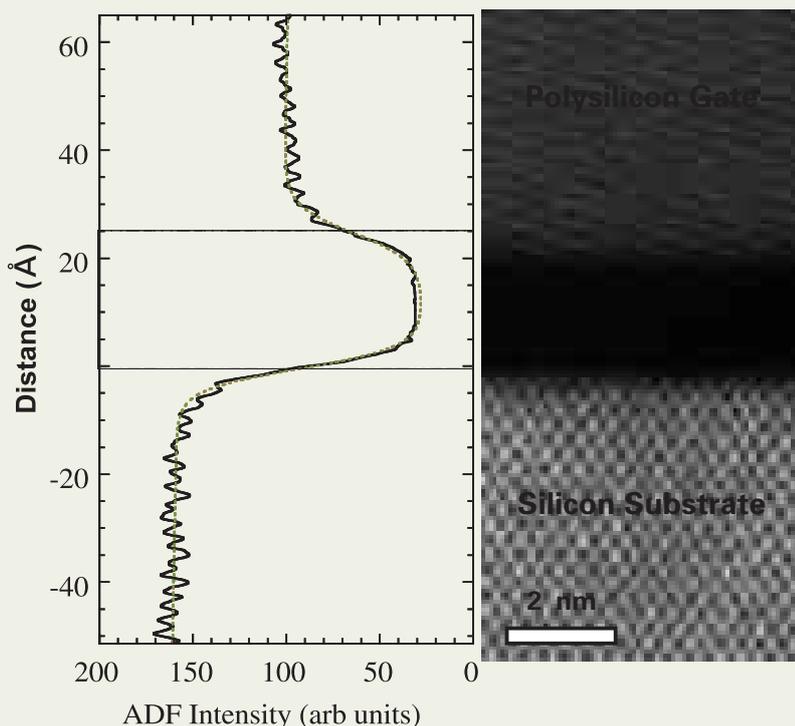19. S. J. Pennycook and D. E. Jesson, *Phys. Rev. Lett*. **64**, 938 (1990).

Fig.6. Quantitatively measuring the thickness of a 2.5 nm gate oxide from an ADF image. The gaussian interface roughness model fit is shown as a dotted line. The lower and upper interface roughnesses were 1.75 Å and 3 Å rms respectively. The inner semi-angle on the ADF detector is 40 mrad and the probe forming aperture was 10 mrad semi-angle. (Digiscan and JEOL 2010F-ARP)

Introduction of New Products

Multi Purpose High Perfomance FE SEM

JSM-6500F

JSM-6500F multi purpose high performance FE SEM is equipped with the newly developed In-Lens Thermal FEG, unique combination of the thermal FEG (Field Emission Electron Gun) and the condenser lens produces high probe current sufficient for EBSP, WDS and CL analysis as well as high magnification image observation and EDS. A high probe current in a very small electron probe size enables one to analyze smaller area.

Small probe diameter attainable at the analytical conditions requiring high probe current : 3.0 nm (Probe current : 5 nA, Accelerating voltage: 15 kV, WD:10 mm)
High resolution : 1.5 nm at 15 kV, 5.0 nm at 1kV
Newly developed In-Lens Thermal FEG : Maximum 200 nA probe current available
Emission noise free, stable probe :
Thermal FEG produces high stability for analytical applications
Multi purpose specimen chamber : Maximum 150 mm diameter specimen
Motorized specimen stage : X-Y-Rotation motorized (5 axes motor control: option)
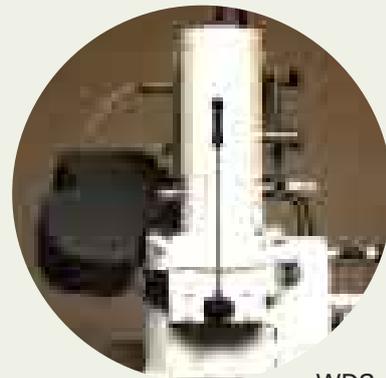One action specimen exchange : Fail safe simple procedure
High Resolution, Crisp Live Image Display : 1,280× 1,024 pixels digital image
Variety of analytical capability : Integrated EDS, WDS, EBSP, CL available as option

EBSP

WDS

EDS

Wafer Surface Particle Analyzers
# JAS-WPA series

The JAS-WPA wafer surface particle analyzer is a laser Raman spectrometer combined with an optical microscope and a defect-review system. Linked with a defect coordinate file obtained by the wafer inspection system, this instrument is capable of not only reviewing defects and particles but also permitting them to be identified by observing the Raman spectra. It can analyze them down to $0.2\,\mu$ m in size and also identify both organic and inorganic compounds effectively. The WPA is a reliable tool that clarifies the cause of occurrence of defects and particles and improves the product yield.

Laser	: Ar+ (wavelength 514.5 nm) standard
Wafer size	: 125 mm, 150 mm, 200 mm
Stage position accuracy	: ± 2.5 mm
Coordinate link	: KLA (KRF), SURFSCAN (tff) and others

Analysis Example

This is an example of analysis of submicron-level particles on a wafer surface. It reveals that a satisfactory spectrum can be obtained by measurement within several tens of seconds. The inclusion in particles is identified as ammonium sulfate $(NH_4)_2SO_4$ by the spectrum collation search with the data base. Even a compound having a complex structure that cannot be identified by element analysis alone can be accurately identified by using the WPA.
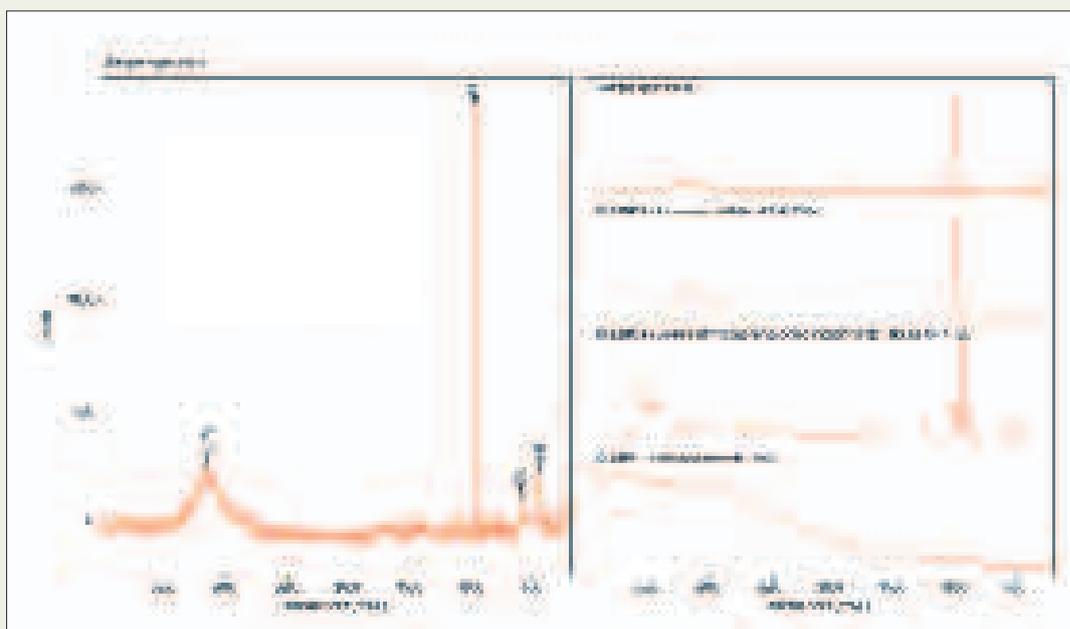
Introduction of New Products

## Mask Observation Scanning Microscope
JWS-7855S

The JWS-7855S has the capability to investigate reticles, X-ray masks, MR Heads and wafers at high specimen stage tilt angles with high resolution. It has a wide range of electron beam accelerating voltages (0.5 kV 15 kV) for both morphological observation and elemental analysis by EDS. It enables the user to make excellent reproducible CD (critical dimension) measurements on flat position of the specimen stage and height CD measurement at 60° as an alternative tool of wafer cross section SEM. When a scheduled program is edited beforehand, the operator is required only to operate a trackball and to control on the operation panel for image observation and schedule program execution. Automatic defect review (ADR) system and automatic defect classification (ADC) system can be integrated for the yield management of semiconductor production lines.

High SEM resolution: 5 nm (1 kV)
High quality SEM images (1280 1024 picls)
Wide range of accelerating voltage (0.5 kV 15 kV)
Stage tilt : −15° to 60° (wafer)
 −15° to 50° (mask)
High throughput
Convenient job schedule functions
Less particle contamination and lower damage

Low accelerating voltage and process monitor analysis application
Tilt : 60°, Acc.v, : 500V
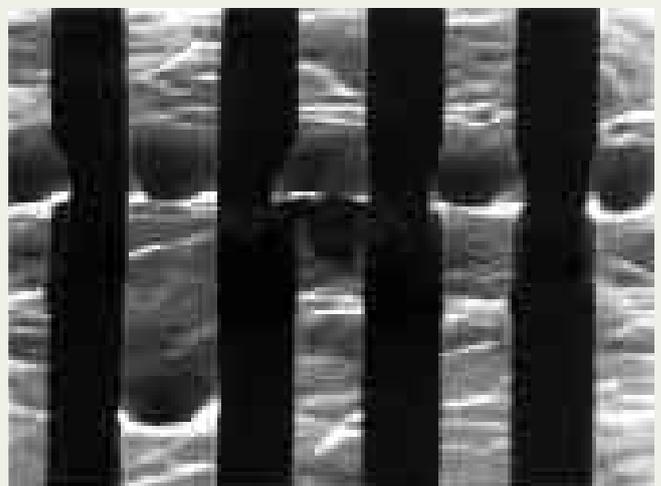
Defect review application at 60° tilt

Dual Beam FIB

JFS-9855S

The JFS-9855S is an upgraded model of JFS-9855 designed as a "CUT and SEE" defect review tool. It allows both in-situ fabrication of defect portion and high resolution SEM observation of the cut section in real time. The capability of quick mode switching between SIM and SEM modes helps to perform "CUT and SEE" analysis very easily. The JFS-9855S can be used as a high-resolution wafer inspection SEM, because it has the column of the JWS-7000 series dedicated to wafer inspection. Another important aspect is the expendability to attach EDS so that it can be used as an analytical SEM.

Automatic defect review (ADR) system and automatic defect classification (ADC) systems can be integrated for the yield management of semiconductor production lines. This system is now applied to the production of many other devices such as MR Head production lines. Thus, the JFS-9855S allows the use as a surface defect analysis tool as well. Such a functional integration will contribute greatly to reduce the time needed for failure analysis, thus allowing quick control in production line.

High SIM resolution : 7 nm (30 kV)
High SEM resolution: 5 nm (1 kV)
High quality SEM images (1,280   1,024 picls)
Stage tilt : 0° to 60° (wafer)
Quick switching between FIB milling and SEI observation modes
Equipped with a C to C auto-loader
Coordinate linkage with optical defect inspection system and laser microscope
Recipe capability for wafer information and observation/milling condition
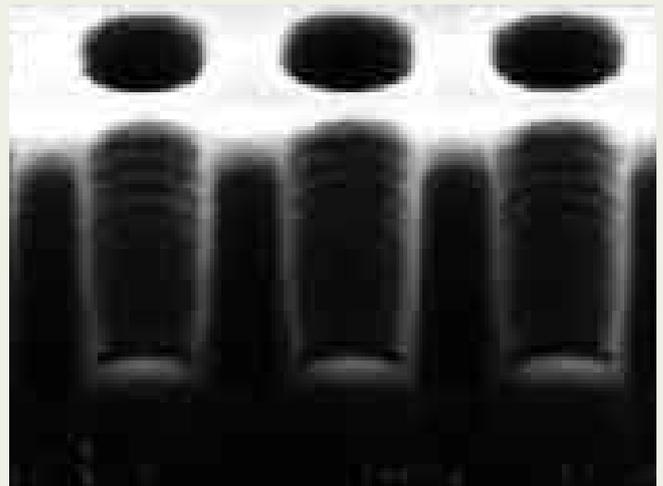
Cross section of contact holes

Cross section of a defect

Kankan diamonds (Guinea): probing the lower mantle

Thomas Stachel[†], Gerhard P. Brey [†] and Jeff W. Harris [††]

[†]Institut für Mineralogie, Universität Frankfurt
[††]Division of Earth Sciences, University of Glasgow

Introduction

Early geophysical observations allowed the distinction of three layers in our Earth, namely the crust with 8 to 50 km thickness, the mantle down to 2900 km and the metallic core (**Fig.1**). Continental and oceanic crust may be studied directly by sampling in deep erosional cuts, dredging from ships and by drilling. Uplifted blocks in the Alps even allow insight into the transition of lower crust to upper mantle. Xenoliths entrained by fast uprising magmas and erupted to the surface by volcanoes allow the study of Earth's mantle material stemming from up to 200 km depth. A quite detailed picture on the chemistry, mineralogy and temperature distribution begins to emerge from these studies. Greater depths and the Earth's core were accessible exclusively to geophysical and high pressure experimental methods. Their results allow the explanation of the most important seismic discontinuities within the Earth's mantle, namely at 410 km and at 660 km (Fig. 1). The 410 km discontinuity marks the transition from the upper mantle (garnet peridotite) with mostly olivine (a Si-poor Mg-silicate Mg_2SiO_4), orthopyroxene (a Si-saturated Mg-silicate $MgSiO_3$) and garnet (a Mg-Al-silicate $Mg_3Al_2Si_3O_{12}$) to the transition zone, where olivine isochemically transforms to a much denser spinel structure and pyroxene increasingly dissolves into garnet (majorite). At 670 km the spinel structured olivine disproportionates into the still denser phase assemblage ferropericlase (MgO) + perovskite structured $MgSiO_3$. Basaltic oceanic crust gets subducted at continental margins and transforms at high pressures first to pyroxene + garnet (eclogite), then, on dissolution of pyroxene into garnet, the entire rock transforms into majorite plus some leftover SiO_2 (stishovite). Majorite exsolves Ca-perovskite ($CaSiO_3$) from about 550 km onwards.

Diamonds grow at depths from about 140 km onwards and inclusions in these diamonds enable us to sample deep regions of our

[†]Senckenberganlage 28, 60054 Frankfurt, Germany

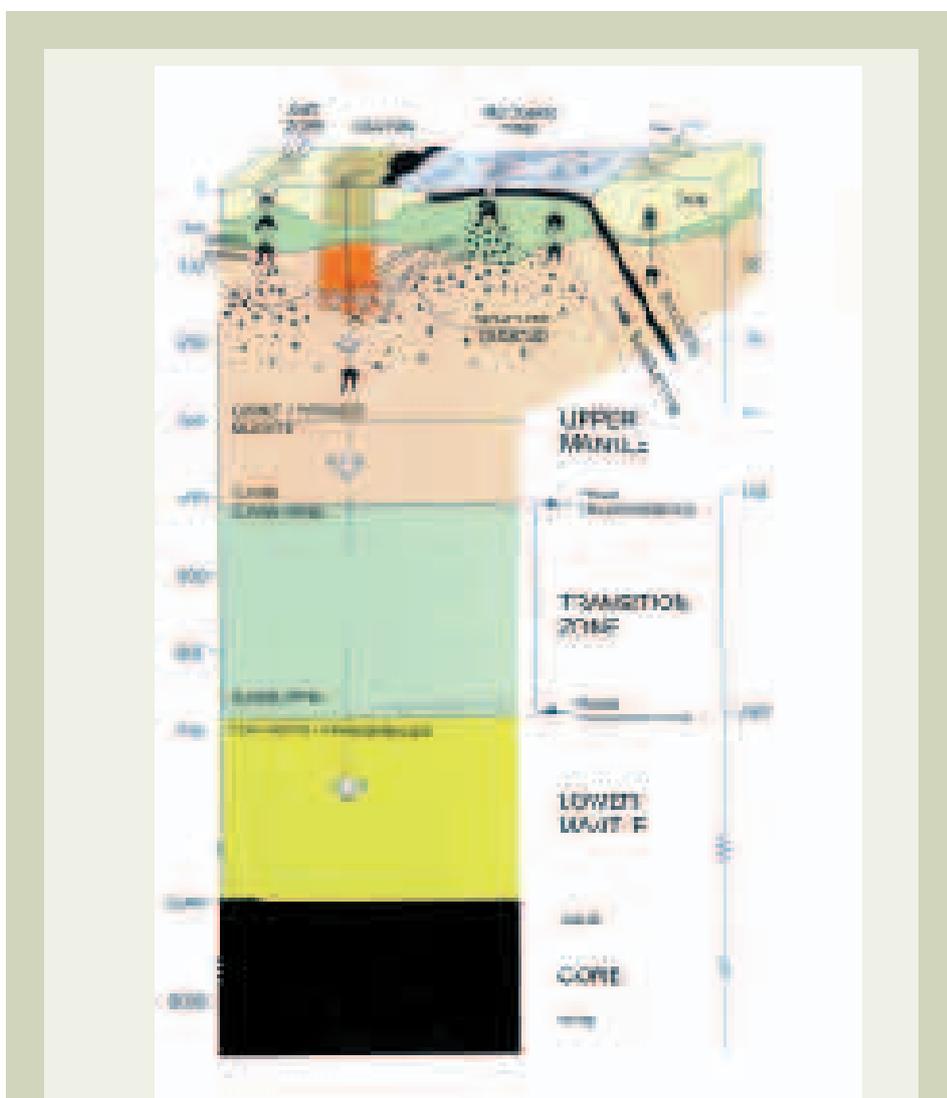E-mail:stachel@em-uni-frankfurt.de
[††]Glasgow G12 8QQ, Scotland, UK

Fig.1. Structure of the Earth showing the major phase transitions at 410 and 660 km, the beginning of the dissolution of pyroxene into garnet to form majorite at 300 km and the resulting division into upper mantle, transition zone and lower mantle and the Earth's core. The lid of the convecting astenosphere is the lithosphere consisting of the continental (yellow) and oceanic (black) crust and the uppermost part of the upper mantle which may be subducted into the mantle below the continents. Diamonds may be brought to the surface from depths exceeding 700 km first by convection and from about 200 km onwards by the explosive force of volcanism.

Earth's mantle. Unequivocal information may be obtained from the inclusions (**Fig. 2**) because they are protected and isolated by a chemically inert container which prevents re-equilibration and retrograde reactions with the surrounding matrix during exhumation.

We have studied diamonds from the Kankan district in Guinea and examined the major and trace element chemistry of "normal" lithospheric inclusion parageneses, diamond populations derived from the asthenosphere and the transition zone (410-660 km) and further lower mantle inclusion parageneses from below 660 km dominated by the mineral ferropericlase. The latter are extremely rare and were described before from only one locality in Brazil.

Samples

In Guinea, diamonds are mined from alluvial deposits in the eastern part of the country. Primary diamond sources are provided by Creta-ceous kimberlite intrusions that range from barren to high diamond grades. In the present study, several thousand Kankan diamonds were examined optically from which 90 diamonds were selected for study of the mineral inclusion content. After breakage, 70 of these diamonds yielded syngenetic mineral inclusions.

Analytical Methods

The small size (between 30 and 100 μm) and the high scientific value of the diamond inclusions require non-destructive microbeam techniques for chemical analysis. For major and trace elements (down to about 100 ppm) the electron microprobe is the obvious choice, as it combines (i) high spatial resolution (at 20 kV gun potentialthe excited sample volume will be about 2 μm (ii) in diameter), high precision and accuracy down to low concentrations and (iii) the ability to check homogeneity of the sample by electron and X-ray images.

Diamond inclusions may be studied in situ by X-ray diffraction for phase identification and structural state. For chemical analysis they need to be released by breaking the diamond. Once released from the host diamond, the inclusions were embedded in araldite® in 5mm brass rings and subsequently polished on a Pb-Sb plate using 1/4 μm diamond powder. EPMA analyses of major elements were performed on a Jeol JXA-8900RL at 20 kV gun potential and 20 nA beam current using silicate, oxide and metal standards. Count times range between 30 and 90 seconds to ensure detection limits of 100 ppm or better for all oxides except SrO and Na$_2$O (200 ppm). Accuracy of major element analyses was checked against secondary standards and is better than 1 % (relative). Analytical precision is mainly controlled by counting statistics (which, for a given oxide species, depend on the concentration) and therefore strongly declines for minor and trace elements.

Fig.2. Inclusions of orange coloured eclogitic garnet (about 250 μm in length) in diamond. Both garnets show a cubo-octa-hedral shape which is imposed by the diamond host and therefore indicative for a syngenetic formation.
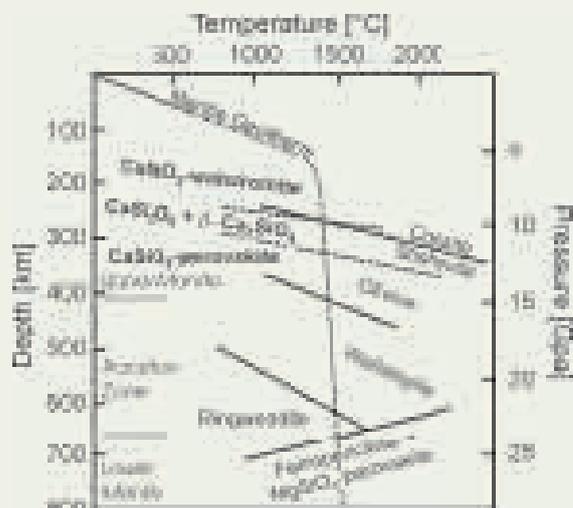

Fig.3. Phase boundaries and reaction curves relevant for the ascent of lower mantle diamonds from Guinea.

At an oxide concentration of 0.10 wt% errors (2 sigma) range between 4-8 % (relative), except for P$_2$O$_5$, NaO and SrO (12-18 %). At the detection limit (0.01-0.02 wt%) errors increase to about 20 % for the majority of oxides, but range between 27-45 % for the latter group.

Composition of Inclusions -

14 diamonds yielded inclusions belonging to the peridotitic suite with garnets, 16 olivines, three clinopyroxenes and four chromites. Representative microprobe analyses are given in **Table 1.**

19 Kankan diamonds are eclogitic from which eleven yielded 12 *eclogitic garnets*. These are mainly high-Ca garnets and six contain a significant majorite component (see Table 1). Majorite component means the solid solution of pyroxene in garnet to form A$^{2+}_4$Si$^{[6]}$Si$^{[4]}_3$O$_{12}$. The molar proportion of the majorite component increases with pressure and may be used to estimate depths of origin (see below). In part, majoritic garnets also show very high sodium contents with Na$_2$O exceeding 1 wt.%. Thirteen *clinopyroxenes* were found in nine eclogitic diamonds. Two coexist with majoritic garnets and show high to very high potassium contents, which are correlated to the Si-excess of their coexisting garnets.

Inclusions of likely lower mantle origin have been released from 34 diamonds. By far the most common inclusion is ferropericlase; a total of 39 inclusions were recovered from 32 diamonds. Kankan ferropericlase is very magnesian, At Kankan, significant impurities in ferropericlase are formed by NiO (0.08-1.46 wt%, av. 1.27 wt%), Cr$_2$O$_3$ (0.01-1.04 wt%, av. 0.55 wt%), Na$_2$O (0.07-0.79 wt%, av. 0.32 wt%) and MnO (0.13-0.26 wt%, av. 0.19 wt%).

Seven *MgSiO$_3$* inclusions were found in four ferropericlase bearing diamonds. Due to the very strong partitioning of Ni into ferropericlase, MgSiO$_3$ inclusions formed in the lower mantle may be readily distinguished from upper mantle orthopyroxenes by very low Ni (0.03 wt% NiO) contents.

Five *CaSiO$_3$* inclusions have been released from four diamonds, all but one coexisting with ferropericlase. XRD showed two of these to have reversed into the walstromite structure (the stable modification of CaSiO$_3$ between 3-10 Gpa (**Fig 3**). In three diamonds bimineralic inclusions of Ca$_2$SiO$_4$-larnite and CaSi$_2$O$_5$-titanite have been identified by in situ XRD. In one case, the inclusion was subsequently released for EPMA and found to show a thin band of CaSiO$_3$ (< 10 μm) separating the other two phases (**Fig. 4**). The phase relationships for CaSiO$_3$ (Gasparik et al. 1994) are consistent with the mineralogical relationships just noted, as CaSiO$_3$-perovskite decomposes to larnite + CaSi$_2$O$_5$-titanite at pressures below 12 GPa before recombining to form CaSiO$_3$-walstromite at pressures below 10 GPa. The three polymineralic Ca-silicate inclusions, therefore, are pressure-inversion reaction products of primary CaSiO$_3$-perovskite.

Compositionally the inclusions are 99 % pure CaSiO$_3$, with minor Al$_2$O$_3$ (0.03-0.66 wt%), SrO (0.06-0.85 wt%) and K$_2$O (0.01-0.73 wt%), which all positively correlate with each other. SiO$_2$ in the form of coesite was also observed in two diamonds containing Ca-silicates, which were examined by XRD only (Joswig et al. 1999). As the stability fields of CaSiO$_3$-perovskite and coesite do not overlap, these SiO$_2$-phases were most likely also included as stishovite. Along an adiabatic geothermal gradient, the phase boundary stishovite-coesite coincides with the reaction curve larnite + CaSi$_2$O$_5$-titanite = CaSiO$_3$-walstromite (Fig.3).

Diamond KK-109 contains (i) two isolated ferropericlase grains with higher Mg/Fe and Cr and lower Ni than (ii) the ferropericlase in contact with olivine which is heterogeneous in Mg/Fe and locally very high in Cr, Al and Ti. These elements correlate positively indicating sub-microscopic Cr-spinel, which is in accordance with the cloudy optical appearance of the olivine. High resolution element mapping yields elongated spots (<<1 μm, **Fig. 5**) with high Al and Cr indicating exsolution of spinel from olivine. From mixing trends of multiple spot analyses we calculate the composition of the spinel exsolution bodies to be about Fe$_{0.37}$Mg$_{0.77}$Cr$_{0.41}$Al$_{1.46}$Ti$_{0.03}$O$_4$. Chemical differences and exsolution features may be explained if olivine is the final reaction product of a primary ferropericlase + MgSiO$_3$-perovskite inclusion with an excess amount of ferropericlase. Upon reaction first to spinel structured -olivine the Ni content in the remaining ferropericlase increases and becomes higher than in the isolated ferropericlases. Also, the Mg/Fe becomes lower and Al, Cr and Ti dissolve in the spinel structure which subsequently exsolve as Cr-spinel during conversion to -olivine. That the reaction of ferropericlase with MgSiO$_3$ did not immediately produce -olivine but first the -phase is indicated further by a strong chemical zonation of the olivine towards the ferropericlase-rim, with the Mg-number increasing from 94.7 to 96.1 and NiO

sample	KK-26a	KK-26b	KK-28b	KK-86	KK-81a	KK-81b	KK-108c	KK-108e	KK-66a
mineral	olivine	garnet	cpx	garnet	garnet	cpx	Fe-periclase	MgSiO$_3$	CaSiO$_3$
paragenesis	peridotitic	peridotitic	peridotitic	eclogitic	deep-ecl.	deep-ecl.	lower mantle	lower mantle	lower mantle
P$_2$O$_5$	0.01	0.01	0.01	0.04	0.05	0.02	0.01	0.01	0.02
SiO$_2$	40.57	42.14	55.03	39.49	45.05	55.21	0.02	57.04	51.08
TiO$_2$	0.01	0.27	0.04	0.72	1.16	0.65	0.01	0.05	0.07
Al$_2$O$_3$	0.02	18.64	0.64	21.31	16.64	6.31	0.06	1.66	0.39
Cr$_2$O$_3$	0.04	5.50	0.74	0.04	0.08	0.05	0.57	0.26	0.02
FeO	8.18	7.10	3.13	20.86	10.32	4.42	22.47	4.87	0.07
MnO	0.12	0.31	0.13	0.42	0.26	0.07	0.20	0.11	0.04
NiO	0.38	0.00	0.08	0.00	0.02	0.04	1.38	0.02	0.01
MgO	50.40	21.23	20.78	8.17	15.18	12.35	75.69	35.00	0.08
CaO	0.04	4.98	17.93	9.15	9.89	14.79	0.01	0.10	47.07
SrO									0.73
Na$_2$O	0.02	0.04	0.59	0.27	1.37	4.05	0.31	0.04	0.07
K$_2$O	0.01	0.01	0.18	0.01	0.01	1.44	0.01	0.01	0.43
Total	99.78	100.21	99.28	100.47	100.02	99.40	100.70	99.16	100.08
P				0.005	0.006	0.001			0.001
Si	0.992	6.042	1.991	6.002	6.558	2.001	0.001	1.968	1.985
Ti		0.029	0.001	0.083	0.127	0.018		0.001	0.002
Al	0.001	3.150	0.027	3.816	2.854	0.270	0.006	0.067	0.018
Cr	0.001	0.623	0.021	0.005	0.009	0.001	0.033	0.007	0.001
Fe^{2+}	0.167	0.851	0.095	2.651	1.257	0.134	1.402	0.141	0.002
Mn	0.003	0.038	0.004	0.054	0.032	0.002	0.013	0.003	0.001
Ni	0.008		0.002		0.003	0.001	0.083	0.000	
Mg	1.836	4.537	1.121	1.851	3.293	0.667	8.418	1.800	0.005
Ca	0.001	0.765	0.695	1.490	1.543	0.574		0.004	1.959
Sr									0.016
Na	0.001	0.012	0.042	0.079	0.386	0.285	0.045	0.002	0.005
K			0.008			0.066			0.021
Total	3.008	16.047	4.008	16.036	16.067	4.020	10.001	3.994	4.016
[O]	4.000	24.000	6.000	24.000	24.000	6.000	10.000	6.000	6.000

Table 1. Representative electron microprobe analyses (in wt%) and calculated atomic proportions of peridotitic, eclogitic and lower mantle inclusions in Kankan diamonds.

decreasing from 0.34 to 0.16 wt%. This is due to diffusion of Fe and Ni into ferropericlase after conversion of the spinel phase into -olivine, since experimentally determined partitioning of Fe/Mg shows significantly lower $D_{Fe/Mg}$ ferropericlase/ -phase relative to ferropericlase/olivine. Our finding here is the first clear evidence of naturally occurring Mg_2SiO_4 spinel in terrestrial materials.

Pressure and Temperature Estimates

Using various geothermometers and geobarometers based on major element compositions of coexisting phases pressures and temperatures of about 5.5 GPa at 1200 °C and up to 7.8 GPa at 1400 °C were estimated for the peridotitic inclusions. These are typical P-T conditions for cratonic regions in other diamond producing areas with an additional contribution of diamonds from unusually great depth (approx. 250 km) which may come close to the base of the lithosphere. The depths of origin of the majoritic garnets may be estimated from their excess Si-content with shows that the deepest majoritic garnet comes from 440 km within the transition zone.

No geothermobarometers are available to determine the PT conditions of formation for lower mantle inclusions. However, a depth of origin may be derived from the composition of the $MgSiO_3$-perovskites based mainly on the Al-content. Various studies show that at 22.5 GPa (at 1630 °C) 1.2-1.9 wt% Al_2O_3 are dissolved and at 24 GPa $MgSiO_3$-perovskite has about 4 wt% Al_2O_3. Therefore, the low aluminium contents of the $MgSiO_3$-perovskites from Kankan (max. 1.7 wt% Al_2O_3) suggest derivation from the uppermost 10-20 km of the lower mantle.

Conclusions

The majoritic inclusion paragenesis is derived from a large depth interval extending approximately from 250 to 440 km, i.e. from the asthenosphere into the transition zone. The lower mantle appears to be the dominant source for Guinea diamonds. Apart from frequent inclusions of ferropericlase, we observed several associations that may only exist at depths exceeding 660 km. Examples are the parageneses of ferropericlase with $CaSiO_3$- and $MgSiO_3$-perovskite and stishovite. The low aluminium contents of the $MgSiO_3$ inclusions indicate derivation from the uppermost decakilometres of the lower mantle.

Several diamonds contain inclusions which are best explained in terms of re-equilibration of former lower mantle parageneses at decreasing pressure and temperature: (i) $CaSiO_3$-perovskites in part decomposed to Ca_2SiO_4-larnite and $CaSi_2O_5$-titanite, which in turn may recombine to $CaSiO_3$-walstromite, (ii) $CaSiO_3$- and $MgSiO_3$-perovskite may react to form clinopyroxene and (iii) $MgSiO_3$-perovskite and ferropericlase form olivine with excess ferropericlase or enstatite. These observations suggest that exhumation from the lower mantle was slow, probably in a rising plume, which allowed adjustment of external pressure on the host diamond and internal pressure on the inclusions via plastic deformation.
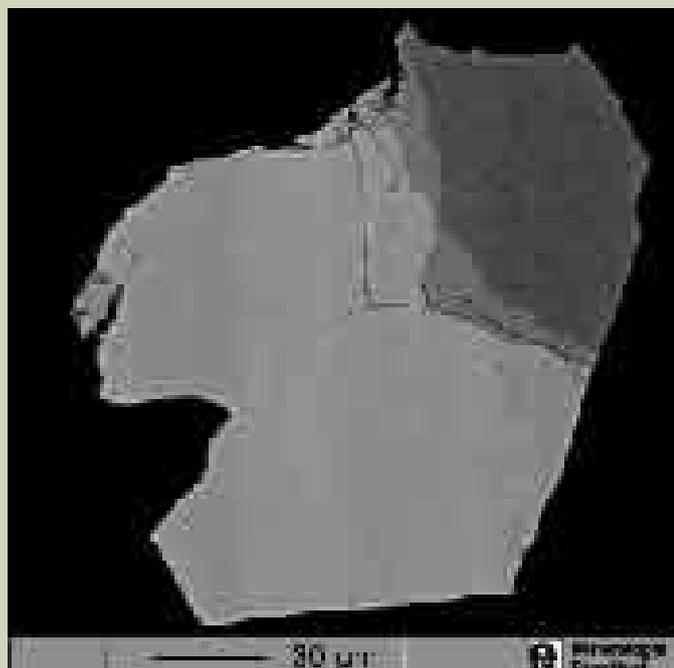

Fig.4. Backscattered electron image of the polished surface of the Ca-silicates in diamond KK-44. Two crystals of larnite (b-Ca_2SiO_4) form the bright coloured left part of the inclusion. The darker coloured upper right consists of $CaSi_2O_5$-titanite. The darker veins within the brecciation are chemically not distinct from the host. The thin grey band separating larnite and $CaSi_2O_5$ consists of $CaSiO_3$.

Fig.5. Wave length dispersive beam scan map showing the distribution of Al in the olivine part of KK-109a. Al concentrations increase from blue through green and yellow to red. Increased Al corresponds to submicroscopic exsolutions of spinel. Note that exsolution features less than 0.2 mm in diameter are clearly recognisable without the need to produce ultra-thin sections for transmission electron microscopy.